Polyhedron 157 (2019) 548–557

Contents lists available at ScienceDirect

Polyhedron

journal homepage: www.elsevier.com/locate/poly

Synthesis of β-ketoiminate and β-iminoesterate tungsten (VI) oxo-alkoxide complexes as AACVD precursors for growth of WO_x thin films

Xiaoming Su, Taehoon Kim, Khalil A. Abboud, Lisa McElwee-White *

Department of Chemistry, University of Florida, Gainesville, FL 32611-7200, USA

ARTICLE INFO

Article history:
Received 31 August 2018
Accepted 13 October 2018
Available online 24 October 2018

Dedicated to Prof. William D. Jones.

Keywords:
Tungsten oxide
Chemical vapor deposition
Single source precursors
metal oxo complexes
metal oxide films

ABSTRACT

The tungsten (VI) oxo-alkoxide complexes $WO(OR)_3L$ [R = ^{t}Bu; L = acNac, etNac, tbNac, acNac^{Me}, acNac^{Et}] (**1**–**5**) and $WO(OCH_3)_3$(acNac) (**6**) have been synthesized. The isomeric purity of these complexes depends on the steric bulk of the substituent on the imino nitrogen of the chelating ligand. The thermal properties of the complexes have been evaluated to assess the effect of the β-ketoiminate or β-iminoesterate ligands. $WO(OC(CH_3)_3)_3$(acNac) (**1**) has been used as a precursor for aerosol assisted chemical vapor deposition (AACVD) of WO_x thin films at temperatures from 250 to 450 °C. The results of mass spectrometry and thermolysis studies have been used to propose possible precursor decomposition pathways during film deposition.

1. Introduction

Tungsten oxide is an extensively investigated functional material for various applications such as electrochromic devices [1,2], sensing [3,4], catalysis [5–7] and organic electronics [8]. Besides the advantages of low cost, good chemical stability and mechanical flexibility, the wide application of tungsten oxide can also be attributed to its variety of phases (structural complexity) and stoichiometries (compositional complexity), which results in unique optical, electrical, photocatalytic and magnetic properties [9]. For example, $WO_{2.5}$ can be applied as an efficient electron and hole injection/transport layer in organic light-emitting diodes (OLEDs) [10], while $WO_{2.72}$ is an efficient catalyst for hydrogenation [5] and $WO_{2.9}$ shows great potential in HCHO sensing and elimination [11,12].

Due to the close relationship between physiochemical structures and materials properties, the ability to control stoichiometry, degree of crystallinity and morphology of WO_x to meet the requirements for specific application is critical. Among the numerous WO_x processing techniques including sol–gel, sputtering and thermal evaporation, chemical vapor deposition finds practical use due to its capability to deliver large-scale conformal coatings. Aerosol-assisted chemical vapor deposition (AACVD) is a variant of conventional CVD in which the precursor is dissolved in a solvent and then delivered to the reactor as an aerosol [13]. Therefore, AACVD relies on the solubility of the precursors instead of volatility, which offers greater flexibility in precursor design [14].

Ideal precursors for CVD would have adequate volatility (or solubility for AACVD), stability during the transport process to the reactor, clean decomposition and easy preparation [15]. Utilizing chelating ligands as a strategy to increase the volatility and stability of tungsten oxide precursors has been reported [16–19]. However, these studies are limited to the use of β-diketonate/β-ketoesterate and aminoalkoxide ligands. The β-ketoiminate/iminoesterate ligands are a very attractive class of mixed N,O-bidentate ligands for preparation of various metal complexes, which have been applied in medicinal chemistry [20], polymerization [21] and MOCVD [22–25]. Apart from easy preparation and good coordination ability, their steric and electronic properties can be tuned by altering the substituents on the backbone or the nitrogen. Due to the limited application of these ligands in designing WO_x precursors, we have synthesized complexes of the type $WO(OR)_3L$ (R = ^{t}Bu, Me) bearing various β-ketoiminate/β-iminoesterate ligands, which include 4-amino-3-penten-2-onate (acNac), 4-(methylamino)-3-penten-2-onate (acNac^{Me}), 4-(ethylamino)-3-penten-2-onate (acNac^{Et}), ethyl 3-aminocrotonate (etNac) and *tert*-butyl 3-aminocrotonate (tbNac) (see Scheme 1). We then studied AACVD of WO_x thin films from $WO(OC(CH_3)_3)_3$(acNac) (**1**). To the best of our knowledge, this the first reported study in

* Corresponding author.
E-mail address: lmwhite@chem.ufl.edu (L. McElwee-White).

https://doi.org/10.1016/j.poly.2018.10.035
0277-5387/

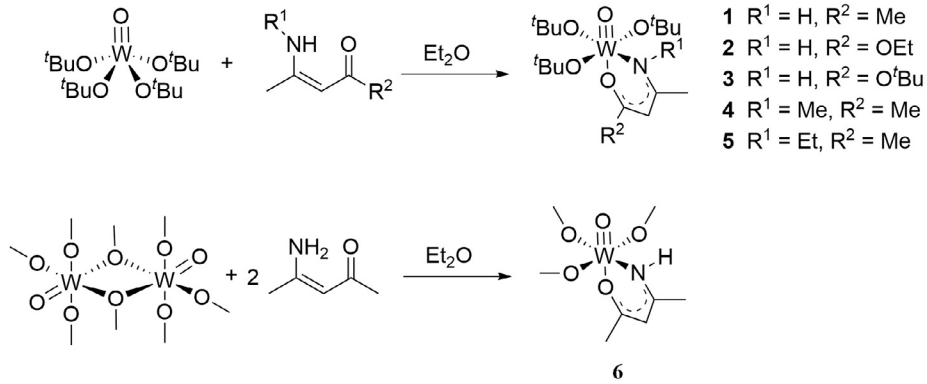

Scheme 1. Synthesis of complexes **1**–**6**.

which the N,O-bonding analogs of acac chelating ligands have been used in precursors for chemical vapor deposition of tungsten oxides.

2. Experimental

2.1. General considerations

All reactions were carried out under an inert atmosphere (N_2) employing conventional glovebox or standard Schlenk techniques. Methylene chloride, hexane and toluene (Fisher Scientific) were purified using an MBraun MB-SP solvent purification system and stored over activated 3 Å molecular sieves prior to use. Diethyl ether and tetrahydrofuran were dried using sodium/benzophenone, distilled, and stored over activated 3 Å molecular sieves prior to use. Hexamethyldisiloxane, methanol, chloroform-d_1 (Cambridge Isotopes) and benzene-d_6 (Cambridge Isotopes) were stored over 4 Å molecular sieves. Diethylamine was distilled over potassium hydroxide and stored over 4 Å molecular sieves. The compounds $WOCl_4$ [26], $WO[OC(CH_3)_3]_4$ [26], $[WO(OCH_3)_4]_2$ [27], acNacH [28], acNac^{Me}H [29], acNac^{Et}H [30], 4-*tert*-butylamino-3-penten-2-one (acNac^{tBu}H) [31], etNacH [28] and tbNacH [28] were synthesized according to literature procedures with modifications. All other solvents and reagents were of analytical grade and were used as received. NMR spectra were recorded on either a Varian Mercury 300BB (300 MHz) spectrometer or a Varian INOVA 500 spectrometer using residual protons from deuterated solvents for reference. Thermogravimetric analysis was performed using a TA Q5000 under an atmosphere of nitrogen at a temperature scan rate of 10 °C/min to 600 °C. Mass spectrometry was performed on a ThermoScientific DSQ II with direct insertion probe (DIP) using chemical ionization (CI) with methane as the reagent gas or electron ionization (EI) (70 eV) or a Bruker Daltonics Impact II-Qq-TOF instrument with electrospray as the source of ionization in positive mode. Elemental analyses were performed by Robertson Microlit Laboratories (Ledgewood, NJ).

2.2. Synthesis

2.2.1. $WO(OC(CH_3)_3)_3$(acNac) (**1**)

In the glove box, $WO(OC(CH_3)_3)_4$ (2.093 mmol, 1.030 g) was dissolved in diethyl ether (30 mL) in a Schlenk flask and then transferred to the Schlenk line. 4-Amino-3-penten-2-one (2.108 mmol, 0.2090 g) was dissolved in diethyl ether (10 mL). The $WO(OC(CH_3)_3)_4$ solution was cooled to 0 °C in ice bath for 30 min, and the solution of 4-amino-3-penten-2-one was then added dropwise. The reaction mixture was then slowly warmed to room temperature after stirring for 30 min. The reaction was allowed to stir for 12 h, then the volatiles were removed under vacuum. The crude product was sublimed between 62 and 74 °C (50–100 mTorr) to obtain yellow solid. Yield: 0.715 g (66.0%). Crystals for X-ray crystallography were grown by cooling a toluene/hexane solution of complex **1** to −3 °C. ^{1}H NMR (C_6D_6, 25 °C): δ 7.13 (b, 1H, NH), 4.75 (d, 1H, CHCO, J = 1.7 Hz), 1.75 (s, 3H, $COCH_3$), 1.59 (s, 9H, C$(CH_3)_3$), 1.44 (s, 18H, C$(CH_3)_3$), 1.32 (d, 3H, CH_3C(NH), J = 1.0 Hz). ^{13}C NMR (C_6D_6, 25 °C): δ 181.26 ($COCH_3$), 168.95 (C(NH)), 99.76 ($CHCO(CH_3)$), 82.48 ($C(CH_3)_3$), 80.62 ($C(CH_3)_3$), 30.22 (($CH_3)_3$C), 30.74 (($CH_3)_3$C), 26.12 (CH_3CO), 25.60 (CH_3C(NH)). *Anal.* Calc. for $WO_5C_{17}H_{35}N$: C, 39.47; H, 6.82; N, 2.71. Found: C, 38.23, H, 6.34; N, 2.75%. MS (ESI) m/z Calcd for $WO_5C_{17}H_{35}NK$ $[M+K]^+$: 556.1657. Found: 556.1634.

2.2.2. $WO(OC(CH_3)_3)_3$(etNac) (**2**)

Compound **2** was synthesized following the same procedure as used for **1**. Starting with $WO(OC(CH_3)_3)_4$ (1.219 mmol, 0.6003 g) and etNacH (1.229 mmol, 0.1588 g), a yellow solid (0.5601 g, 84.0%) was obtained after removal of the volatiles under vacuum. The crude product was sublimed at 52–62 °C (100–140 mTorr) to afford a yellow product. Yield: 0.1425 g (23.5%). ^{1}H NMR (C_6D_6, 25 °C): δ 6.41 (b, 1H, NH), 4.66 (d, 1H, CHCO, J = 1.6 Hz), 4.04 (q, 2H, CH_2CH_3, J = 7.1 Hz), 1.56 (s, 9H, C$(CH_3)_3$), 1.45 (s, 18H, C$(CH_3)_3$), 1.33 (s, 3H, CH_3C(NH)), 1.06 (t, 3H, CH_3CH_2, J = 7.1 Hz). ^{13}C NMR (C_6D_6, 25 °C): δ 170.96 ($COCH_2$), 168.89 (C(NH)), 82.98 ($CHCOCH_2$), 82.02 ($C(CH_3)_3$), 81.01 ($C(CH_3)_3$), 60.39 (CH_2CH_3), 31.05 (($CH_3)_3$C), 30.72 (($CH_3)_3$C), 26.19 (CH_3C(NH)), 15.01 (CH_3-CH_2). MS (ESI) m/z Calcd for $WO_6C_{18}H_{37}NK$ $[M+K]^+$: 586.1762. Found: 586.1781.

2.2.3. $WO(OC(CH_3)_3)_3$(tbNac) (**3**)

Compound **3** was synthesized following the same procedure as used for **1**. Starting with $WO(OC(CH_3)_3)_4$ (1.015 mmol, 0.4998 g) and tbNacH (1.023 mmol, 0.1608 g), a yellow solid (0.4422 g, 75.7%) was obtained after removal of the volatiles under vacuum. The crude product was sublimed at 59–62 °C (220–380 mTorr) to afford a yellow product. Yield: 0.1124 g (19.2%). ^{1}H NMR (C_6D_6, 25 °C): δ 6.27 (b, 1H, NH), 4.60 (d, 1H, CHCO, J = 1.6 Hz), 1.57 (s, 9H, C$(CH_3)_3$), 1.50 (s, 9H, $COC(CH_3)_3$), 1.44 (s, 18H, C$(CH_3)_3$), 1.32 (d, 3H, CH_3C(NH), J = 0.6 Hz). ^{13}C{^{1}H} NMR (C_6D_6, 25 °C): δ 171.78 ($COC(CH_3)_3$), 168.74 (C(NH)), 84.45 ($CHCOC(CH_3)_3$), 81.55 ($C(CH_3)_3$), 80.90 ($C(CH_3)_3$), 79.83 ($OC(CH_3)_3$), 31.06 (($CH_3)_3$C), 30.74 (($CH_3)_3$C), 29.16 (($CH_3)_3$C), 25.78 (CH_3C(NH)). MS (ESI) m/z Calcd for $WO_6C_{20}H_{41}NK$ $[M+K]^+$: 615.210. Found: 615.2129.

2.2.4. $WO(OC(CH_3)_3)_3$(acNac^{Me}) (**4**)

Compound **4** was synthesized following the same procedure as used for **1**. Starting with $WO(OC(CH_3)_3)_4$ (2.099 mmol, 1.0333 g) and acNac^{Me}H (2.105 mmol, 0.2382 g), a yellow solid (0.8806 g, 79.0%) was obtained after removal of the volatiles under vacuum.

The crude product (**4A** with traces of **4B**) was sublimed at 82–94 °C (100–200 mTorr) to afford a yellow solid, which is a mixture of **4A** and **4B** in ~1:3 ratio. Yield of the mixture: 0.5383 g (48.3%). Isomer **4A**: ^{1}H NMR (C_6D_6, 25 °C): δ 4.85 (s, 1H, CHCO), 3.10 (s, NCH_3), 1.86 (s, 3H, $COCH_3$), 1.58 (s, 9H, $C(CH_3)_3$), 1.48 (s, 18H, $C(CH_3)_3$), 1.45 (s, 3H, $CH_3C(NCH_3)$). ^{13}C NMR (C_6D_6, 25 °C): δ 170.34 ($COCH_3$), 167.26 ($C(NCH_3)$), 104.21 ($CHCO(CH_3)$), 82.56 ($C(CH_3)_3$), 80.96 ($C(CH_3)_3$), 39.50 ($N(CH_3)$), 30.97 (($CH_3)_3C$), 30.27 (($CH_3)_3C$), 25.07 (CH_3CO), 21.41 ($CH_3C(NCH_3)$). Isomer **4B**: ^{1}H NMR (C_6D_6, 25 °C): δ 4.89 (s, 1H, CHCO), 3.41 (s, NCH_3), 1.77 (s, 3H, $COCH_3$), 1.58 (s, 9H, $C(CH_3)_3$), 1.43 (s, 18H, $C(CH_3)_3$), 1.40 (s, 3H, $CH_3C(NCH_3)$). ^{13}C NMR (C_6D_6, 25 °C): δ 177.57 ($COCH_3$), 168.62 ($C(NCH_3)$), 104.03 ($CHCO(CH_3)$), 82.72 ($C(CH_3)_3$), 80.41 ($C(CH_3)_3$), 43.33 ($N(CH_3)$), 31.16 (($CH_3)_3C$), 30.75 (($CH_3)_3C$), 25.22 (CH_3CO), 21.92 ($CH_3C(NCH_3)$). *Anal.* Calc. for $WO_5C_{18}H_{37}N$ (mixture of **4A** and **4B**): C: 40.69; H: 7.02; N: 2.64. Found: C, 40.30; H, 6.77; N, 2.63%.

2.2.5. $WO(OC(CH_3)_3)_3(acNac^{Et})$ (**5**)

Compound **5** was synthesized following the same procedure as used for **1**. Starting with $WO(OC(CH_3)_3)_4$ (1.623 mmol, 0.7988 g) and $acNac^{Et}H$ (1.640 mmol, 0.2086 g), a yellow oil (0.5192 g, 58.7%) was obtained after removal of the volatiles under vacuum. The crude product was distilled at 82–90 °C (100–200 mTorr) to afford a yellow oil. Yield: 0.2895 g (32.7%). The isomer ratio of **5A** and **5B** is ~1:1 and they were not separated from one another. For the mixture of **5A** and **5B**: ^{1}H NMR (C_6D_6, 25 °C): δ 4.85 (s, 1H, CHCO), 4.77 (s, 1H, CHCO), 3.85 (q, NCH_2CH_3, J = 7.1 Hz), δ 3.57 (q, NCH_2CH_3, J = 7.1 Hz), 1.82 (s, 3H, $COCH_3$), 1.75 (s, 3H, $COCH_3$), 1.58 (s, 9H, $C(CH_3)_3$), 1.55 (s, 9H, $C(CH_3)_3$), 1.54 (s, 3H, $CH_3C(NC_2H_5)$), 1.53 (s, 3H, $CH_3C(NC_2H_5)$), 1.45 (s, 18H, $C(CH_3)_3$), 1.41 (s, 18H, $C(CH_3)_3$), 1.33 (t, NCH_2CH_3, J = 7.1 Hz), 1.16 (t, NCH_2CH_3, J = 7.1 Hz). ^{13}C NMR (C_6D_6, 25 °C): δ 177.10 ($COCH_3$), 169.24 ($COCH_3$), 168.09 ($C(NC_2H_5)$), 165.60 ($C(NC_2H_5)$), 104.01 ($CHCO(CH_3)$), 103.51 ($CHCO(CH_3)$), 82.67 ($C(CH_3)_3$), 82.40 ($C(CH_3)_3$), 81.02 ($C(CH_3)_3$), 80.70 ($C(CH_3)_3$), 50.18 ($N(CH_2CH_3)$), 46.09 ($N(CH_2CH_3)$), 31.08 (($CH_3)_3C$), 30.97 (($CH_3)_3C$), 30.85 (($CH_3)_3C$), 30.26 (($CH_3)_3C$), 25.32 (CH_3CO), 25.08 (CH_3CO), 21.62 ($CH_3C(NC_2H_5)$), 21.19 ($CH_3C(NC_2H_5)$), 16.39 ($N(CH_2CH_3)$), 15.42 ($N(CH_2CH_3)$). *Anal.* Calc. for $WO_5C_{19}H_{39}N$: C: 41.85; H: 7.21; N: 2.57. Found: C, 41.52; H, 7.21; N, 2.66%.

2.2.6. $WO(OCH_3)_3(acNac)$ (**6**)

Compound **6** was synthesized following the same procedure as used for **1**. Starting with $[WO(OCH_3)_4]_2$ (0.771 mmol, 0.4998 g) and acNacH (1.572 mmol, 0.1558 g), a yellow solid (0.4952 g, 82.0%) was obtained after removal of the volatiles under vacuum. The crude product was distilled at 70–74 °C (100–140 mTorr) to afford a yellow oil. Yield: 0.1695 g (28.1%). ^{1}H NMR (C_6D_6, 25 °C): δ 7.36 (b, 1H, NH), 4.68 (s, 3H, OCH_3), 4.63 (d, 1H, CHCO, J = 1.9 Hz), 4.41 (s, 6H, OCH_3), 1.75 (s, 3H, $COCH_3$), 1.18 (d, 3H, $CH_3C(NH)$, J = 0.8 Hz). $^{13}C\{^1H\}$ NMR (C_6D_6, 25 °C): δ 182.40 ($COCH_3$), 171.30 (C(NH)), 100.87 ($CHCO(CH_3)$), 63.41 (OCH_3), 61.77 (OCH_3), 26.07 (CH_3), 25.55 (CH_3). *Anal.* Calc. for $WO_5C_8H_{17}N$: C: 24.57; H: 4.38; N: 3.58. Found: C, 24.36; H, 4.21; N, 3.61%.

2.3. WO_x materials growth and characterization

WO_x films were deposited onto silicon substrates with native silicon dioxide (Si/SiO_2, n-type, <100>) using a custom-built, vertical cold-wall impinging-jet AACVD reactor [32]. Substrates were cleaned in boiling acetone, ethanol and deionized water for 3 min each, and then placed on a SiC covered graphite susceptor in the reaction chamber under vacuum. Solutions of precursor **1** (0.034 M in diglyme) were prepared and loaded into a 10 mL gas-tight Hamilton syringe (4 mL h^{-1} injection rate). Aerosol was generated from the precursor solution using a nebulizer with a quartz plate vibrating at 1.44 MHz and delivered to the reaction chamber with nitrogen (99.999% purity, Airgas) carrier gas at a flow rate of 1000 sccm. Deposition was conducted for 150 min, during which the reactor pressure was maintained at 350 Torr and the deposition temperature was controlled by a radio frequency (RF) heating system on the susceptor.

The elemental composition of WO_x films was determined using ULVAC-PHI XPS Al Kα radiation after 2 min 2 kV Ar^+ sputtering to remove surface contaminants and oxygen was used as an internal standard set at 530.5 eV [16,33]. The Shirley base line was subtracted before peak fitting. The XPS spectra of the W 4f core level were fitted into peak doublets with parameters of spin–orbit separation ΔEP ($4f_{5/2}$–$4f_{7/2}$) = 2.18 eV. The intensity ratio of the W $4f_{7/2}$ and W $4f_{5/2}$ peak doublet was set to 4:3. The morphology of the films was examined using field emission scanning electron microscopy (FESEM, FEI Nova NanoSEM 430). The crystallinity was measured by X-ray diffraction (XRD, Panalytical X'pert Pro).

2.4. Crystallographic structure determination of **1**

X-ray Intensity data were collected at 100 K on a Bruker **DUO** diffractometer using Mo Kα radiation (λ = 0.71073 Å) and an APEXII CCD area detector. Raw data frames were read by the program SAINT[1] and integrated using 3D profiling algorithms. The resulting data were reduced to produce *hkl* reflections and their intensities and estimated standard deviations. The data were corrected for Lorentz and polarization effects and numerical absorption corrections were applied based on indexed and measured faces.

The structure was solved and refined in *SHELXTL2014*, using full-matrix least-squares refinement. The non-H atoms were refined with anisotropic thermal parameters and all of the H atoms were calculated in idealized positions and refined riding on their parent atoms. The asymmetric unit consists of two crystallographically independent but chemically equivalent complexes. The amino proton from both complexes were obtained from a Difference Fourier map and refined freely. The second complex (W1b) has two disordered regions. In one, the three methyl groups bound to C10b are refined in two parts. In the second, the full ligand on O3b is refined in two parts as well. In both cases the site occupation factors were dependently refined. In the final cycle of refinement, 9941 reflections (of which 9078 are observed with $I > 2\sigma(I)$) were used to refine 483 parameters and the resulting R_1, wR_2 and S (goodness of fit) were 2.72%, 5.51% and 1.064%, respectively. The refinement was carried out by minimizing the wR_2 function using F^2 rather than F values. R_1 is calculated to provide a reference to the conventional R value but its function is not minimized.

2.5. Thermolysis studies

Each compound (complex **1**, **2** and pure ligand acNacH) was placed in a 10 mL headspace vial with a septum and heated in the GC oven at 250 °C for 40 min. The oven was then cooled to 32 °C. Once cool, the headspace vial was removed from the oven. A 100-μL sample of the headspace gases was taken with a gas-tight syringe and injected in split mode for GC/MS. Mass spectrometry was conducted on a ThermoScientific (San Jose, CA) DSQ II using electron ionization (70 eV) and an ion source at 250 °C. Gas chromatography was conducted on a ThermoScientific Trace GC Ultra.

2.6. Adhesion test

The Scotch tape test was used to evaluate the adhesion of the deposited WO_x films on native silicon dioxide (Si/SiO_2, n-type, <100>) substrates. A strip of commercial Scotch tape (Magic™, 3M) was attached to the deposited film and then peeled off. The film adhered to the substrate and not to the tape. Images of the

tape and the films before and after the test are in supplementary information (Fig. S8).

3. Results and discussion

3.1. Precursor design

Compounds of the type $WO(OR)_3L$ (R = alkyl; L = β-diketonate, β-ketoesterate) have been studied as WO_x CVD precursors [16,17] but the research on tungsten complexes containing the structurally related β-ketoiminate or β-iminoesterate ligands has been very limited. β-Ketoiminates or β-iminoesterates have been successfully used as ligands in CVD precursors for metal oxide films including MgO [34], ZnO [35] and Co_3O_4 [36]. In contrast to the commonly used β-diketonate ligands, these mixed N/O chelating ligands provide more flexibility for controlling the physical and thermal properties of the complexes by tuning the substituents at the imino functionality or the backbone. Oxo and alkoxide groups have advantageous features in synthesizing single source metal oxide precursors. As O-bound ligands, they can serve as the oxygen source for materials growth. Tungsten-oxygen multiple bonding in the oxo ligands reduces bond cleavage requirements during deposition. Bulky *tert*-butoxide and the smallest alkoxide methoxide have been chosen as ligands in this study, to allow exploration of the influence of steric bulk and mixed N/O chelating ligands.

3.2. Synthesis

β-Ketoimines and β-iminoesters were synthesized by condensation reactions between the corresponding β-diketone/β-ketoester and a suitable amine source according to modified literature procedures [28,30]. The mononuclear complexes $WO(OR)_3L$ (R = alkyl, L = β-ketoiminate or β-iminoesterate) were prepared by addition of the bidentate ligand to $[WO(OMe)_4]_2$ or $WO(O^tBu)_4$ in ether (Scheme 1). After reacting at room temperature for 12 h, all volatiles were removed to give the crude product, which can be further purified by sublimation or distillation. Attempts to synthesize and purify $WO(OMe)_3L$ complexes where L = $acNac^{Me}$ or $acNac^{Et}$ failed, due to rapid decomposition of the products. The reactivity of β-ketoiminate ligands towards tungsten oxo alkoxide complexes is significantly affected by the steric bulk of their imino side chains. The N-^{t}butyl compound $acNac^{tBu}H$ does not react with $WO(O^tBu)_4$ or $[WO(OMe)_4]_2$ even at elevated temperature with increased reaction time.

3.3. X-Ray crystallographic structure determination of **1**

Single crystals of complex **1** that were suitable for molecular structure determination (Table 1) were grown by cooling a concentrated solution of **1** in toluene layered with hexane to −3 °C. There are two crystallographically independent but chemically equivalent molecules per asymmetric unit. One of the molecules is presented in Fig. 1. Selected bond angles and lengths are given in Table 2. Complex **1** exhibits a distorted octahedral geometry around the metal center with an equatorial plane defined by a *tert*-butoxide, the terminal oxo and the bidentate β-ketoiminate ligand. The other two chemically equivalent *tert*-butoxide ligands occupy non-linear axial positions (O5B-W1B-O3B, 163.96(16)°) bending away from the terminal oxo group. Besides the effect of steric repulsion, the distortion of normal octahedral geometry is also influenced by the strong multiple bonding of W–O(oxo), which is facilitated by the restricted bite angle of the chelating β-ketoiminate ligand (O2B-W1B-N1B, 79.41(13)°) [17,37].

Despite the possibility of isomers due to the unsymmetrical nature of the acNac ligand, complex **1** shows an exclusive *trans* geometry between the oxo ligand and O (O,O-*trans*) due to the *trans* effect of W–O(oxo) [37–39]. Compared with compounds of the type $[WO(OR)_3(acac)]$, whose W–O bonds trans to the oxo groups are typically ~2.2 Å [17], the analogous W1B–O2B bond

Table 1
Crystal data and structure refinements for **1**.

Empirical formula	$C_{17}H_{35}NO_5W$
Formula weight	517.31
Temperature	100(2) K
Wavelength	0.71073 Å
Crystal system	triclinic
Space group	$P\bar{1}$
Unit cell dimensions	
a (Å)	10.4335(6)
b (Å)	13.5435(7)
c (Å)	15.4896(8)
α (°)	95.753(1)
β (°)	95.922(1)
γ (°)	92.651(1)
V (Å^3)	2162.6(2)
Z	4
D_{calc} (Mg/m^3)	1.589
Absorption coefficient (mm^{-1})	5.364
F(0 0 0)	1032
Crystal size (mm)	0.221 × 0.095 × 0.044
Theta range for data collection (°)	1.906–27.499
Index ranges	$-13 \le h \le 13$, $-17 \le k \le 17$, $-20 \le l \le 20$
Reflections collected	61 410
Independent reflections (R_{int})	9941 (0.0166)
Completeness to theta = 25.242°	100.0%
Absorption correction	numerical
Refinement method	Full-matrix least-squares on F^2
Data/restraints/parameters	9941/504/483
Goodness-of-fit (GOF) on F^2	1.064
Final R indices [$I > 2\sigma(I)$]	R_1 = 0.0272, wR_2 = 0.0551 [9078]
R indices (all data)	R_1 = 0.0310, wR_2 = 0.0579
Extinction coefficient	n/a
Largest difference peak and hole (e Å^{-3})	5.508 and −3.202
$R_1 = \sum(\|\|F_o\| - \|F_c\|\|)/\sum\|F_o\|$	$wR_2 = [\sum[w(F_o^2 - F_c^2)^2]/\sum(w(F_o^2)^2]]^{1/2}$
$S = [\sum[w(F_o^2)^2 - F_c^2)^2]/(n\text{-}p)]^{1/2}$	$w = 1/[\sigma^2(F_o^2) + (m^*p)^2 + n^*p]$
$p = [\max(F_o^2,0) + 2^*F_c^2]/3$, m & n are constants	

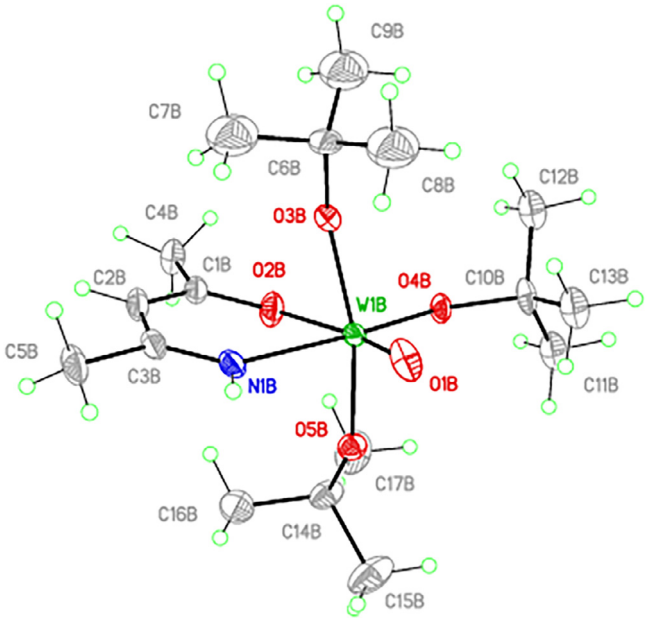

Fig. 1. A representation of **1** with thermal displacement ellipsoids shown at 40%.

Table 2
Selected bond distances (Å) and angles (°) for complex **1**.

Bond parameter		Bond Parameter	
W1B–O1B	1.727(3)	W1B–O2B	2.084(3)
W1B–O3B	1.897(4)	W1B–O4B	1.880(3)
W1B–O5B	1.893(3)	W1B–N1B	2.175(3)
C1B–C2B	1.369(6)	C2B–C3B	1.414(6)
O5B–W1B–O3B	163.96(16)	O2B–W1B–N1B	79.41(13)
O4B–W1B–N1B	169.50(13)	O1B–W1B–O4B	103.84(13)
O1B–W1B–O2B	165.90(13)	O1B–W1B–N1B	86.62(14)

distance (2.084(3) Å) for complex **1** is significantly shorter. Although solid state pure acNacH appears to be more enaminoketone than enol [40], the C2B-C3B bond of **1** (1.414(6) Å) is noticeably longer than the C1B–C2B bond (1.369(6) Å). These bond lengths are consistent with the enolate being the major resonance contributor to the overall complex structure.

3.4. NMR spectroscopy

In the ^{1}H NMR spectra of **1**–**6**, there are two sets of symmetry inequivalent *tert*-butoxide signals in a 2:1 intensity ratio, which shows that the complexes are all *mer* isomers. According to the NMR spectra, only one isomer of compounds **1**–**3** and **6** was formed. In contrast, the NMR spectra of **4** and **5** indicate the presence of two isomers. Due to the unsymmetrical nature of the chelating ligand, there are two possible *mer* isomers of [WO(OR)$_3$L] (L = β-ketoiminate or β-iminoesterate) complexes: O,O-*trans* and O,N-*trans*. For compounds **1**–**3** and **6**, the oxygen is *trans* to the terminal oxo, as favored by the *trans* effect of the W-O(oxo) unit. The O,O-*trans* geometries of **2**, **3** and **6** were inferred from the crystallographic structure of **1**, which indicates the O,O-*trans* isomer instead of O,N-*trans*. In contrast to the single isomers of **1**–**3** and **6**, compounds **4** and **5**, which are N-alkylated, are formed as a pair of isomers. For the crude product before sublimation, ^{1}H NMR indicates that **4A** is the major isomer with the presence of traces of **4B** (<5%). After sublimation, **4B** is the major component of the mixture (**4A** ~25%, **4B** ~75%). These results are consistent with isomerization of the kinetic product **4A** (O,O-*trans*) to the thermodynamic product **4b** (O,N-*trans*) as the mixture is heated during sublimation. For compound **5**, which has a somewhat larger N-alkyl group than **4** (ethyl vs. methyl), both the crude and distilled product of compound **5** are composed of **5A** and **5B** in a roughly 1:1 ratio.

For compounds **1**–**3** and **6**, a long-range H—H coupling is observed: H^b is a doublet coupled with H^a ($^4J_{HH} \approx 1.6$ Hz) (Scheme 2). This long range coupling is not observed in the ^{1}H NMR spectrum of the free ligand and is attributed to the "W" geometry enforced when the bidentate ligand is coordinated with tungsten [41].

3.5. Thermogravimetric analysis

The thermal properties of compounds **1**–**3** and **6** were studied using thermogravimetric analysis (Fig. 2). All compounds display stepwise decomposition with major mass loss from the initial heating stage until 200 °C. Compounds **1**–**3** bearing large *tert*-butoxide ligands show a larger mass loss rate below 150 °C compared with methoxide complex **6**, which is consistent with early loss of *tert*-butyl groups. Compounds **2** and **3**, which have β-iminoesterate ligands, start to decompose at lower temperatures than β-ketoiminate complexes **1** and **6**, indicating that β-iminoesterate ligands can provide easier decomposition pathways. This observation is similar to our previous finding during the study of complexes WO(OR)$_3$L (R = alkyl; L = β-ketoesterates, β-diketonates) that β-ketoesterates offer more facile fragmentations involving

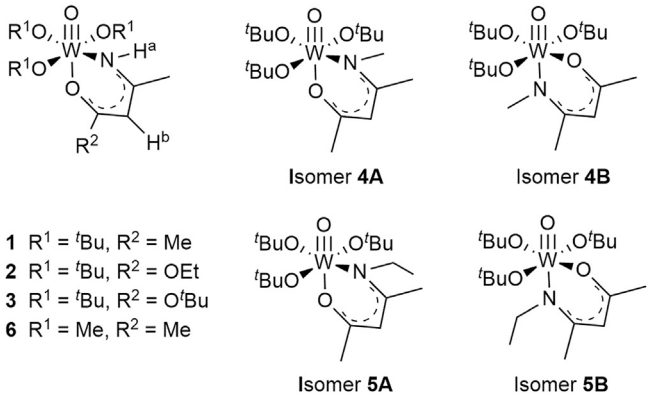

Scheme 2. Structures of compounds **1**–**6**.

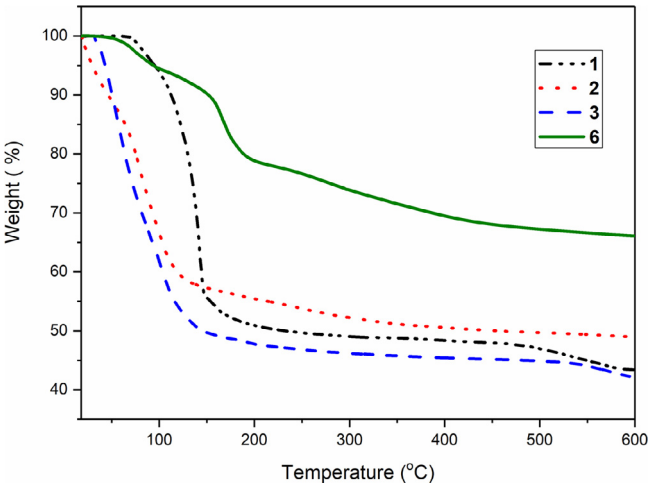

Fig. 2. Thermogravimetric analysis plots for compounds **1**–**3** and **6**.

the ester group when compared with β-diketonates [16]. The observed residual masses of complexes **1** and **3** are nearly identical to the calculated residual mass of WO_3, implying clean decomposition to the oxide. Complexes **2** and **6** have higher residual mass than the calculated WO_3 percentage (Table 3), consistent with some incorporation of material from the ligands into the final pyrolyzed product. The difference between the residual mass and the calculated WO_3 percentage from **1**-**3** and **6** demonstrates that *tert*-butyl groups (**1** and **3**) provide easier fragmentation and cleaner decomposition compared with methyl and ethyl derivatives (**2** and **6**). The comparison of compound **1** and **6**, which only differ from each other in the steric bulk of alkoxides, demonstrates that the application of sterically crowded ligands can improve the thermal behavior of precursors [42].

3.6. Mass spectrometry

Mass spectrometry (MS) has been utilized to study deposition mechanisms of CVD precursors [43–45]. Careful interpretation of

Table 3
Actual residual mass and the calculated WO_3 percentage for compounds **1**–**3** and **6**.

	Residual mass (%)	Calculated WO_3 percentage (%)
1	43	45
2	49	42
3	42	40
6	66	59

Table 4
Selected fragments observed in positive ion mass spectra of **1**–**3** and **6**.

$WO(OR)_3L$	$[M\text{-}HOR+K/H]^+$ *m/z* (%)	$[M\text{-}L]^+$ *m/z* (%)	$[M\text{-}OR\text{-}R+H/K]^+$ *m/z* (%)	$[M\text{-}L\text{-}R+H/K)]^+$ *m/z* (%)	$[M\text{-}OR\text{-}HOR]^+$ *m/z* (%)
$WO(O^tBu)_3$(acNac) (**1**)[a]	466.4 (100)	419.2 (51)	388.3 (27)	363.3 (83)	n.o.[d]
$WO(O^tBu)_3$(etNac) (**2**)[b]	512.1 (91)	n. o.	456.0 (61)	401.0 (10)	n.o.
$WO(O^tBu)_3$(tbNac) (**3**)[b]	502.2 (77)	419.1 (29)	446.1 (32)	363.1 (44)	n.o.
$WO(OMe)_3$(acNac) (**6**)[c]	360.0 (100)	293.0 (67)	n.o.	n.o.	328.0 (83)

Compounds were analyzed by (a) DIPCI, (b) ESI-MS/MS, (c) DIPEI, (d) n.o. = not observed.

mass spectrometry data is required because the ionic fragments observed in MS are not the neutral species commonly produced upon thermolysis under film growth conditions [43,44]. Selected ions observed in positive ion mass spectra of **1**–**3** and **6** are shown in Table 4. In tandem ESI mass spectrometry for **2** and **3**, $[M+K]^+$ for compound **2** and $[M+H]^+$ for compound **3** were selected as the parent ions to undergo further fragmentation. Fragmentation patterns show that decomposition can start with a loss of alkoxide or the chelating ligand. The higher abundance of $[M\text{-}OR]^+$ than $[M\text{-}L]^+$ suggests more lability of alkoxides than β-ketoiminate/β-iminoesterate ligands, which is not surprising given the chelating nature of the latter. The ions $[M\text{-}OR\text{-}R+H/K]^+$ and $[M\text{-}L\text{-}R+H/K)]^+$ observed for compounds **1**–**3** indicate pathways for dealkylation of a *tert*-butoxide ligand to generate a second oxo group, leading to the formation of tungsten dioxo species as previously observed for the complexes $WO(OR)_3L$ (R = Np, ^{t}Bu, $C(CH_3)_2CF_3$, $C(CF_3)_2CH_3$; L = β-ketoesterate) [16,17]. The chelating ligand or a *tert*-butoxide group can be protonated from an adjacent *tert*-butoxide functionality with a loss of *tert*-butanol/HL and isobutylene to generate $WO_2(OR)_2$ species. For compound **6**, $[M\text{-}OR]^+$ can lose MeOH through protonation of methoxide by the imino proton to generate $[M\text{-}OR\text{-}HOR]^+$ which is illustrated in Scheme 3.

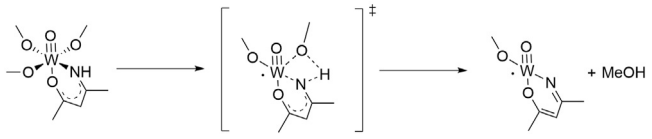

Scheme 3. Proposed decomposition mechanism based on the presence of $[M\text{-}OR\text{-}HOR]^+$ for compound **6**.

3.7. Thermolysis studies

Each compound **1** and **2** was heated in an airtight vial and the volatile decomposition fragments were analyzed by GC–MS. In comparison with mass spectrometry, thermolysis explores how precursors decompose when heated and the connection to CVD is more straightforward. Major fragments and their abundance for each compound are shown in Scheme 4. The identification of isobutylene, *tert*-butanol and acetone provides insight into the decomposition mechanism for the *tert*-butoxide ligand. During thermolysis, the *tert*-butoxide ligand may abstract a proton to give *tert*-butanol and isobutylene, which converts the alkoxide ligand into a second oxo moiety. This finding is consistent with the presence of $[M\text{-}OR]^+$ and $[M\text{-}OR\text{-}R+H/K]^+$ ions in mass spectrometry. The *tert*-butoxyl radical can also decompose to give acetone and a methyl radical [46]. The higher abundance of acetone fragments for compound **1** compared with compound **2** is attributed to decomposition of the acNac ligand to certain extent. The thermolysis of free acNacH yields acetone as its major fragmentation product (99.76%). The presence of ethanol in the decomposition products from compound **2** shows that the β-iminoesterate ligand introduces an additional decomposition pathway in which protonation of the ester alkyl-oxygen is followed by a loss of alcohol.

3.8. Characterization of WO_x films

Tungsten oxide films were grown by AACVD on silicon <100> substrates at 250, 300, 350, and 450 °C using complex **1** as the precursor. The Scotch tape test demonstrated robust adhesion of WO_x films grown at various temperatures on Si substrates (Fig. S8). The films grown at 250 °C were blue while the films grown at higher

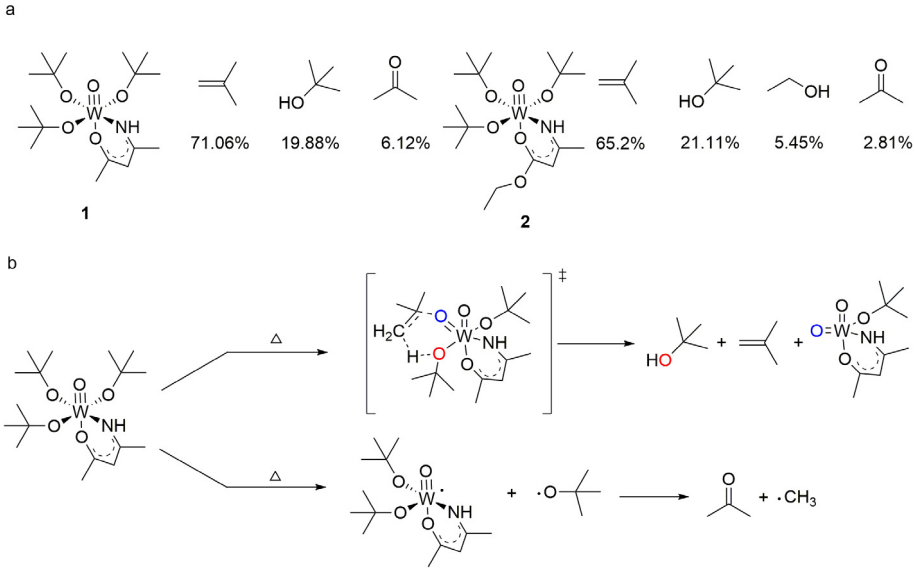

Scheme 4. (a) Thermolysis products of compounds **1** and **2**; (b) proposed decomposition mechanism.

temperatures also had some yellow tint. According to XPS analysis, all the films had good coverage of the substrates with no Si (≤0.1 at %) detected in samples grown from 250 to 350 °C and a small amount of Si (≤3 at%) detected in samples grown at 450 °C. This result is consistent with our previous study using β-diketonate/β-ketoesterate tungsten (VI) oxo-alkoxides in that a small amount of the substrate elements could be detected in films deposited at and above 450 °C [33]. The plane-view SEM images of tungsten oxide films are shown in Fig. 3. The materials grown at 250 °C are amorphous with no texture observed. The films grown at 300 °C appear to have scattered large grains, 200–300 nm in size, which indicates a transition from amorphous films to polycrystalline structures. As the temperature increases to 350 and 450 °C, tungsten oxides with grain-like morphology are deposited. The grain size is significantly reduced with the increase in deposition temperature.

X-ray photoelectron spectroscopy (XPS) was used to determine the composition of the films grown from precursor **1**. The elemental compositions and stoichiometric values are reported in Fig. 4. Nitrogen (≤3 at%) was not detected as a significant component of the deposits at any of the deposition temperatures. The C 1s binding energies (BE) are within the range of 284.5 ± 0.5 eV, suggesting that C is free rather than bound to W or O [33,47]. The as-deposited films grown at 250 °C had an O:W ratio of 2.58. After the films were sputtered using 2 kV Ar^+ source for 2 min to remove surface contaminants, a relatively low O:W ratio of 1.46 was observed. Although an additional 2 min of sputtering only caused the W and O composition to vary within a small range (<0.6 at%), the

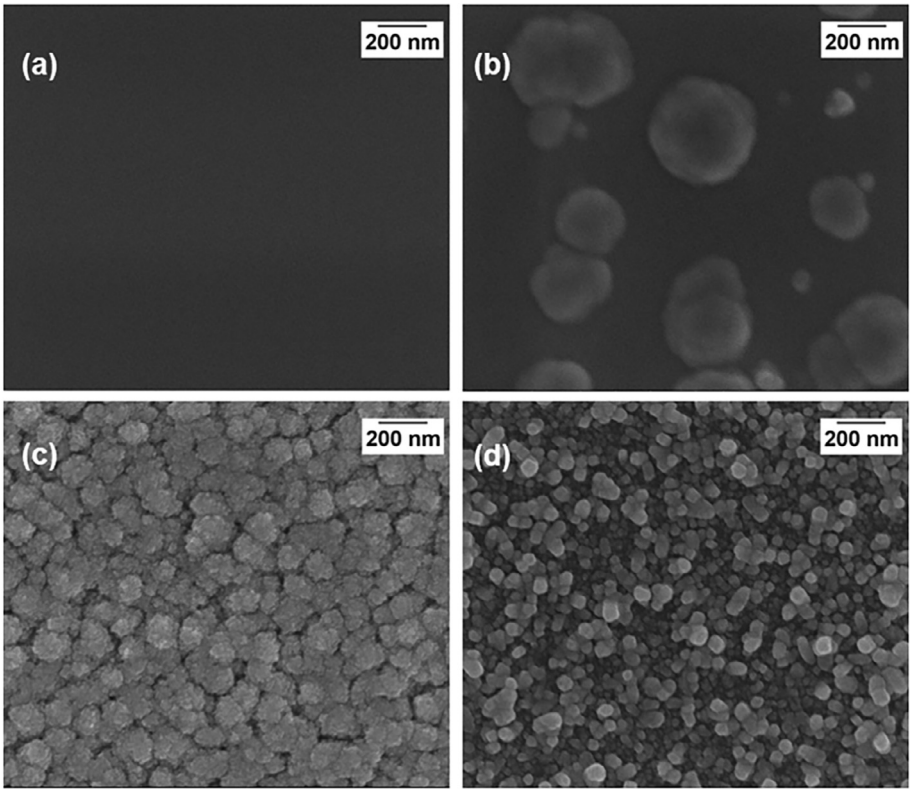

Fig. 3. Plane-view SEM images of samples grown on Si <100> at (a) 250, (b) 300, (c) 350 and (d) 450 °C from precursor **1** dissolved in diglyme using N_2 as carrier gas.

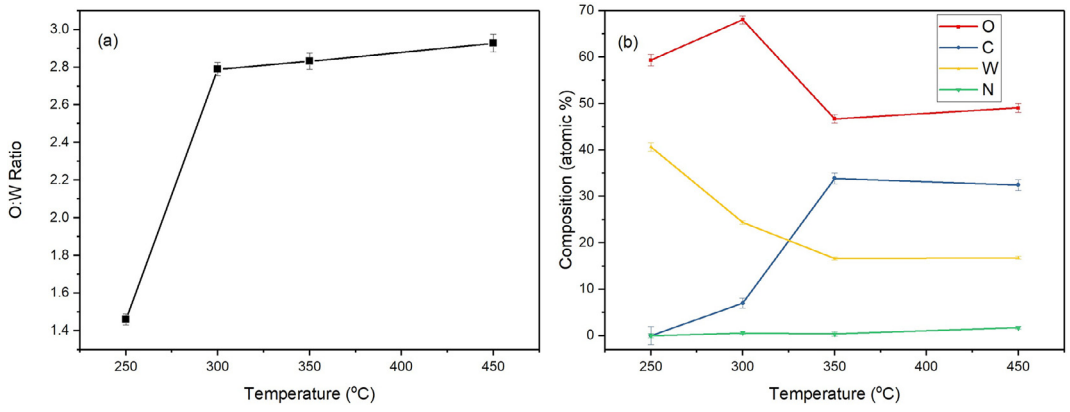

Fig. 4. (a) Overall W, O, C, and N elemental fractions and (b) O:W atomic ratio variation derived from XPS data vs. deposition temperature for samples grown from precursor **1**.

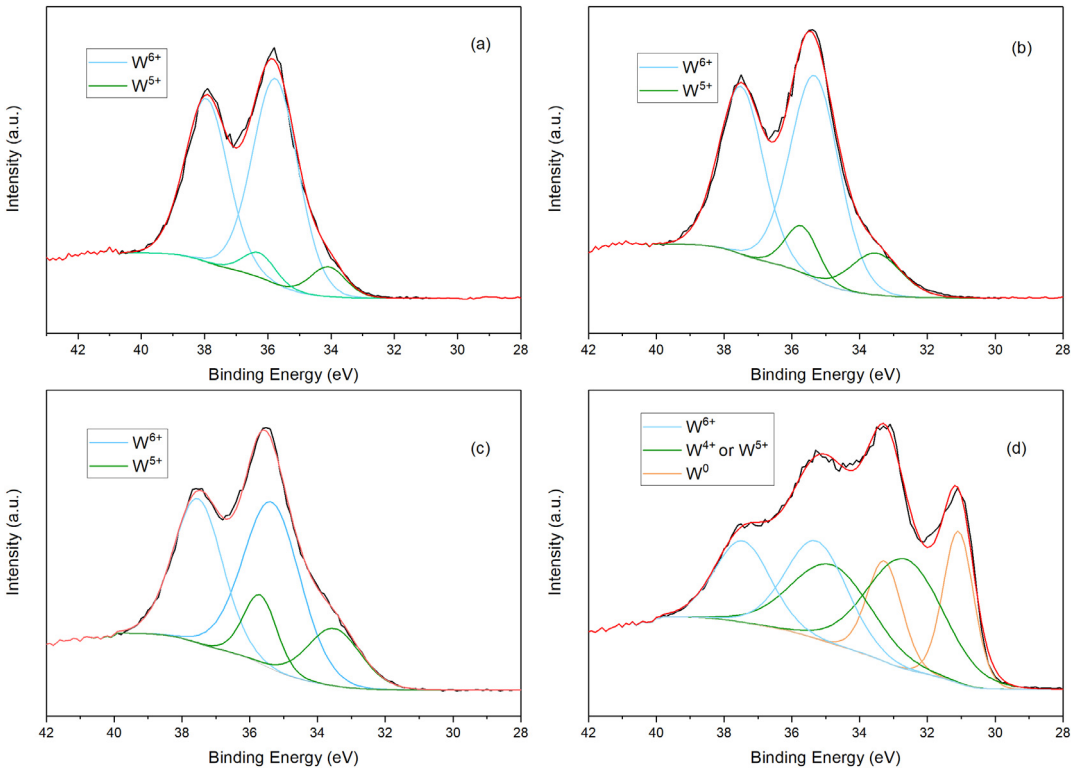

Fig. 5. Deconvolution of W 4f core-level spectra for samples grown from precursor **1** at (a) 450 °C; (b) 350 °C; (c) 300 °C and (d) 250 °C after sputtering. Note: XPS data of as-deposited WO_x films are available in supplementary information (Fig. S11).

measurements are consistent with preferential O sputtering at the deposit surface [48]. There is a rapid increase of O:W ratio to 2.79 when the deposition temperature was elevated to 300 °C. With further increase of growth temperature from 300 to 450 °C, the O:W ratio increases slowly ranging from 2.79 to 2.92. The W 4f core-level spectra for samples grown at different temperatures were deconvoluted to determine the oxidation state of tungsten in the films (Fig. 5). The curves of the W 4f core level spectra for films grown from 300 to 450 °C could be fitted with two spin–orbit doublets, attributed to W^{6+} (W $4f_{7/2}$: 35.5 ± 0.3 eV) and W^{5+} (W $4f_{7/2}$: 33.8 ± 0.3 eV) of W atoms [49,50]. Films grown at higher temperatures demonstrate a greater preference for the higher valent W^{6+} tungsten state compared with W^{5+}. The W 4f spectrum for deposits grown at 250 °C can be deconvoluted into three doublet peaks with binding energies for W $4f_{7/2}$ peak at 35.3 eV, 32.7 eV and 31.1 eV, which corresponds to W^{6+}, W^{4+} or W^{5+}, and W^0.

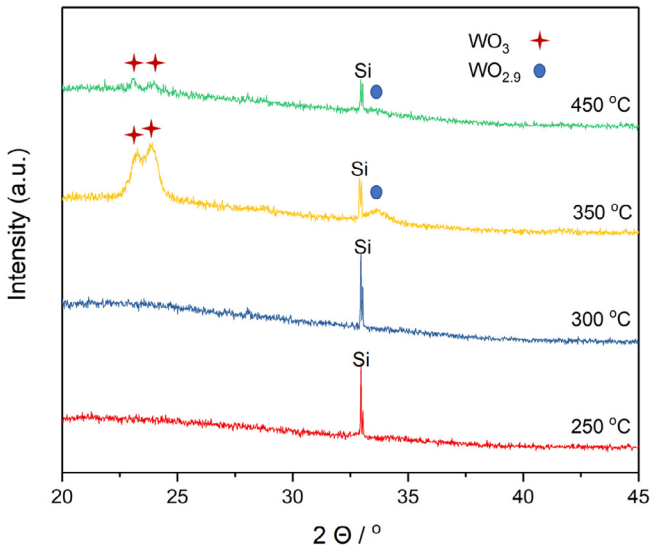

Fig. 6. XRD patterns for samples grown from precursor **1**.

XRD patterns were acquired for the deposited films (Fig. 6). The patterns from films deposited at 250 and 300 °C are featureless with only Si reflections from the substrate evident. The diffraction peaks at 23.1 and 24.0° 2θ for films deposited at 350–450 °C are assigned to crystalline WO_3 (JCPDS card no. 20-1324) with 33.7° 2θ assigned to non-stoichiometric $WO_{2.9}$ (JCPDS card no. 18-1417). These tungsten oxides can be characterized by their unique colors. Stoichiometric WO_3 is yellow and sub-stoichiometric $WO_{2.9}$ is blue. These deposited films have tints of blue and yellow when viewed from different angles, which suggests coexistence of both WO_3 and $WO_{2.9}$ phases.

4. Conclusion

Tungsten (VI) oxo-alkoxide complexes $WO(OR)_3L$ bearing β-ketoiminate or β-iminoesterate ligands have been synthesized, characterized and evaluated as AACVD precursors for deposition of WO_x films. The steric bulk of the substituent on the imino nitrogen of the chelating ligand influences the population of O,O-*trans* and O,N-*trans* isomers of these complexes. Possible mechanisms for formation of W-O(oxo) bonds by loss of alcohols and HL during deposition are consistent with the results of mass spectrometry and thermolysis studies. Non-stoichiometric WO_x films were deposited from compound **1** via AACVD. Films grown at 300–450 °C show O:W ratios ranging from 2.79 to 2.92, while the films grown at 250 °C have a significantly lower O:W ratio. Powder X-ray diffraction demonstrates that deposits grown at temperatures of 350 °C and above contain the crystalline phases of WO_3 and $WO_{2.9}$. Further growth studies with other complexes (e.g., **2**–**6**)

would help to clarify how the incorporation of nitrogen content is influenced by different N-containing precursors and deposition conditions. The electronic and chemical properties of WO_x films are affected by the concentrations of nitrogen doping, thus control of the N content could facilitate potential applications in photocatalysis and photochromism.

Acknowledgements

Mass spectrometry was performed at the Mass Spectrometry Research and Education Center at University of Florida, supported by grant NIH S10 OD021758-01A1. We thank Duane Bock, Frank Schreffler, Nathan Richey and Will Carden for their assistance with materials characterization.

Appendix A. Supplementary data

CCDC 1862469 contains the supplementary crystallographic data for **1**. These data can be obtained free of charge via http://www.ccdc.cam.ac.uk/conts/retrieving.html, or from the Cambridge Crystallographic Data Centre, 12 Union Road, Cambridge CB2 1EZ, UK; fax: (+44) 1223-336-033; or e-mail: deposit@ccdc.cam.ac.uk. Supplementary data to this article can be found online at https://doi.org/10.1016/j.poly.2018.10.035.

References

[1] C.G. Granqvist, Electrochromics for smart windows: Oxide-based thin films and devices, Thin Solid Films 564 (2014) 1.
[2] C.G. Granqvist, Electrochromic tungsten oxide films: Review of progress 1993–1998, Sol. Energy Mater. Sol. Cells 60 (2000) 201.
[3] H.W. Long, W. Zeng, H. Zhang, Synthesis of WO_3 and its gas sensing: a review, J. Mater. Sci.-Mater. Electron. 26 (2015) 4698.
[4] W. Cheng, Y.R. Ju, P. Payamyar, D. Primc, J.Y. Rao, C. Willa, D. Koziej, M. Niederberger, Large-area alignment of tungsten oxide nanowires over flat and patterned substrates for room-temperature gas sensing, Angew. Chem. Int. Edit. 54 (2015) 340.
[5] J.J. Song, Z.F. Huang, L. Pan, J.J. Zou, X.W. Zhang, L. Wang, Oxygen-deficient tungsten oxide as versatile and efficient hydrogenation catalyst, ACS Catal. 5 (2015) 6594.
[6] N. Zhang, X.Y. Li, Y.F. Liu, R. Long, M.Q. Li, S.M. Chen, Z.M. Qi, C.M. Wang, L. Song, J. Jiang, Y.J. Xiong, Defective tungsten oxide hydrate nanosheets for boosting aerobic coupling of amines: synergistic catalysis by oxygen vacancies and bronsted acid sites, Small 13 (2017).
[7] Y.J. Yun, J.R. Araujo, G. Melaet, J. Baek, B.S. Archanjo, M. Oh, A.P. Alivisatos, G.A. Somorjai, Activation of tungsten oxide for propane dehydrogenation and its high catalytic activity and selectivity, Catal. Lett. 147 (2017) 622.
[8] M. Vasilopoulou, G. Papadimitropoulos, L.C. Palilis, D.G. Georgiadou, P. Argitis, S. Kennou, I. Kostis, N. Vourdas, N.A. Stathopoulos, D. Davazoglou, High performance organic light emitting diodes using substoichiometric tungsten oxide as efficient hole injection layer, Org. Electron. 13 (2012) 796.
[9] J. Meyer, S. Hamwi, M. Kroger, W. Kowalsky, T. Riedl, A. Kahn, Transition metal oxides for organic electronics: energetics, device physics and applications, Adv. Mater. 24 (2012) 5408.
[10] M. Vasilopoulou, L.C. Palilis, D.G. Georgiadou, A.M. Douvas, P. Argitis, S. Kennou, L. Sygellou, G. Papadimitropoulos, I. Kostis, N.A. Stathopoulos, D. Davazoglou, Reduction of tungsten oxide: a path towards dual functionality utilization for efficient anode and cathode interfacial layers in organic light-emitting diodes, Adv. Funct. Mater. 21 (2011) 1489.
[11] D.D. Wang, D.X. Han, L. Liu, L. Niu, Sub-stoichiometric $WO_{2.9}$ for formaldehyde sensing and treatment: a first-principles study, J. Mater. Chem. A 4 (2016) 14416.
[12] F.J. Han, F.H. Li, S.W. Liu, L. Niu, Sub-stoichiometric $WO_{2.9}$ as co-catalyst with platinum for formaldehyde gas sensor with high sensitivity, Sens. Actuators, B 263 (2018) 369.
[13] C.Y. Xu, M.J. Hampden-Smith, T.T. Kodas, Aerosol-assisted chemical-vapor-deposition (AACVD) of Binary Alloy (Ag_xPd_{1-X}, Cu_xPd_{1-X}, Ag_xCu_{1-X}) films and studies of their compositional variation, Chem. Mater. 7 (1995) 1539.
[14] P. Marchand, I.A. Hassan, I.P. Parkin, C.J. Carmalt, Aerosol-assisted delivery of precursors for chemical vapour deposition: expanding the scope of CVD for materials fabrication, Dalton Trans. 42 (2013) 9406.
[15] A.C. Jones, Molecular design of improved precursors for the MOCVD of electroceramic oxides, J. Mater. Chem. 12 (2002) 2576.
[16] D.C. Bock, N.C. Ou, R.O. Bonsu, C.T. Anghel, X. Su, L. McElwee-White, Synthesis of tungsten oxo fluoroalkoxide complexes $WO(OR)_3L$ as precursors for growth of WO_x nanomaterials by aerosol-assisted chemical vapor deposition, Solid State Ionics 315 (2018) 77.
[17] R.O. Bonsu, D.C. Bock, H. Kim, R.Y. Korotkov, K.A. Abboud, T.J. Anderson, L. McElwee-White, Synthesis and evaluation of κk^2-β-diketonate and β-ketoesterate tungsten(VI) oxo-alkoxide complexes as precursors for chemical vapor deposition of WO_x thin films, Dalton Trans. 45 (2016) 10897.
[18] C.K. Molloy, A.P. Williams, AACVD of WO_3 thin films from $WO(OPr^i)_3[(O(CH_2)_nNMe_2]$ (n = 2,3), Appl. Organomet. Chem. 22 (2008) 676.
[19] D. Baxter, H.M. Chisholm, S. Doherty, E.N. Gruhn, Chemical vapour deposition of electrochromic tungsten oxide films employing volatile tungsten(VI) oxo alkoxide/beta-diketonate complexes, Chem. Commun (1996) 1129.
[20] R. Pettinari, C. Pettinari, F. Marchetti, C.M. Cavel, R. Scopelliti, P.J. Dyson, Cytotoxicity of ruthenium-arene complexes containing beta-ketoamine ligands, Organometallics 32 (2013) 309.
[21] X.H. He, Y.Z. Yao, X. Luo, J.K. Zhang, Y.H. Liu, L. Zhang, Q. Wu, Nickel(II) complexes bearing N, O-chelate ligands: Synthesis, solid-structure characterization, and reactivity toward the polymerization of polar monomer, Organometallics 22 (2003) 4952.
[22] A. Bastianini, G.A. Battiston, F. Benetollo, R. Gerbasi, M. Porchia, Synthesis and crystal structure of zirconium complexes with fluorinated tetradentate beta-ketoiminate ligands, Polyhedron 16 (1997) 1105.
[23] D.B. Studebaker, D.A. Neumayer, B.J. Hinds, C.L. Stern, T.J. Marks, Encapsulating bis(β-ketoiminato) polyethers. Volatile, fluorine-free barium precursors for metal-organic chemical vapor deposition, Inorg. Chem. 39 (2000) 3148.
[24] S.D. Cosham, G. Kociok-Kohn, A.L. Johnson, J.A. Hamilton, M.S. Hill, K.C. Molloy, R. Castaing, Synthesis and characterization of fluorinated -ketoiminate zinc precursors and their utility in the AP-MOCVD growth of ZnO:F, Eur. J. Inorg. Chem. 4362–4372 (2015).
[25] E. Lay, Y.H. Song, Y.C. Chiu, Y.M. Lin, Y. Chi, A.J. Carty, S.M. Peng, G.H. Lee, New CVD precursors capable of depositing copper metal under mixed O_2/Ar atmosphere, Inorg. Chem. 44 (2005) 7226.
[26] H.J. Wengrovius, R.R. Schrock, Synthesis and characterization of tungsten oxo neopentylidene complexes, Organometallics 1 (1982) 148.
[27] W. Clegg, J.R. Errington, P. Kraxner, C. Redshaw, Solid state and solution studies of tungsten (VI) oxotetraalkoxides, J. Chem. Soc. Dalton Trans. 1431–1438 (1992).
[28] M. Litvic, M. Filipan, I. Pogorelic, I. Cepanec, Ammonium carbamate; mild, selective and efficient ammonia source for preparation of β-amino-α,β-unsaturated esters at room temperature, Green Chem. 7 (2005) 771.
[29] F. Strube, S. Rath, J. Mattay, Functionalized Fulgides and Fluorophore-Photoswitch Conjugates, Eur. J. Org. Chem. 4645–4653 (2011).
[30] A.V. Korolev, V.R. Pallem, Synthesis of copper(II) complexes with diketiminate and ketoiminate, US Patent, US8692010B1 (2014)
[31] S.J.W. Cummins, H.P. Fraser, J.R. Fulton, M.P. Coles, C.M. Fitchett, Coordination of β-ketoimine-derived ligands at main group and transition metals, Aust. J. Chem. 68 (2015) 641.
[32] K.R. McClain, C. O'Donohue, Z. Shi, A.V. Walker, K.A. Abboud, T. Anderson, L. McElwee-White, Synthesis of $WN(NMe_2)_3$ as a precursor for the deposition of WN_x nanospheres, Eur. J. Inorg. Chem. (2012) 4579.
[33] H. Kim, R.O. Bonsu, D.C. Bock, N.C. Ou, R.Y. Korotkov, L. McElwee-White, T.J. Anderson, Tungsten oxide film and nanorods grown by aerosol-assisted chemical vapor deposition using κ^2-β-diketonate and β-ketoesterate tungsten (VI) oxo-alkoxide precursors, ECS J. Solid State Sci. Technol. 5 (2016) Q3095.
[34] J.S. Matthews, O. Just, B. Obi-Johnson, W.S. Rees, CVD of MgO from a $Mg(\beta\text{-ketoiminate})_2$: preparation, characterization, and utilization of an intramolecularly stabilized, highly volatile, thermally robust precursor, Chem. Vap. Deposition 6 (2000) 129.
[35] J.A. Manzi, C.E. Knapp, I.P. Parkin, C.J. Carmalt, Aerosol-assisted chemical-vapour deposition of zinc oxide from single-source β-iminoesterate precursors, Eur. J. Inorg. Chem. (2015) 3658.
[36] K.J. Puring, D. Zywitzki, D.H. Taffa, D. Rogalla, M. Winter, M. Wark, A. Devi, Rational development of cobalt β-ketoiminate complexes: alternative precursors for vapor-phase deposition of spinel cobalt oxide photoelectrodes, Inorg. Chem. 57 (2018) 5133.
[37] M.B. Hursthouse, S.A.A. Jayaweera, A. Quick, Crystal and molecular-structure of [acetone benzoylhydrazonido(1-)-N′O]dichloro-oxo(triphenylphosphine) rhenium(V), J. Chem. Soc.-Dalton Trans. (1979) 279.
[38] G. Lyashenko, G. Saischek, M.E. Judmaier, M. Volpe, J. Baumgartner, F. Belaj, V. Jancik, R. Herbst-Irmer, N.C. Mosch-Zanetti, Oxo-molybdenum and oxo-tungsten complexes of Schiff bases relevant to molybdoenzymes, Dalton Trans. (2009) 5655.
[39] V. Manivannan, J.T. Hoffman, V.L. Dimayuga, T. Dwight, C.J. Carrano, A comparison of vanadyl acetylacetonate complexes of N_2O heteroscorpionate ligands that vary systematically in donor set, Inorg. Chem. Acta 360 (2007) 529.
[40] P.A. Stabnikov, G.I. Zharkova, I.A. Baidina, S.V. Tkachev, V.V. Krisyuk, I.K. Igumenov, Synthesis and properties of a new ketoiminate derivative of the 2,2,6,6-tetramethylheptane-3,5-dionate ligand to prepare volatile CVD precursors, Polyhedron 26 (2007) 4445.
[41] P. Crews, J. Rodríguez, M. Jaspars, Organic Structure Analysis, Oxford University Press, Oxford, New York, 2010.
[42] L. McElwee-White, Design of precursors for the CVD of inorganic thin films, Dalton Trans. (2006) 5327.
[43] Y.S. Won, Y.S. Kim, T.J. Anderson, L.L. Reitfort, I. Ghiviriga, L. McElwee-White, Homogeneous decomposition of aryl- and alkylimido precursors for the chemical vapor deposition of tungsten nitride: a combined density functional theory and experimental study, J. Am. Chem. Soc. 128 (2006) 13781.

[44] Y.S. Won, Y.S. Kim, T.J. Anderson, L. McElwee-White, Computational study of the gas phase reactions of isopropylimido and allylimido tungsten precursors for chemical vapor deposition of tungsten carbonitride films: implications for the choice of carrier gas, Chem. Mater. 20 (2008) 7246.
[45] Y. Yamamoto, S. Inoue, Y. Matsumura, Thermal decomposition products of various carbon sources in chemical vapor deposition synthesis of carbon nanotube, Diam. Relat. Mater. 75 (2017) 1.
[46] K.U. Ingold, The reaction of tert-butoxy radicals with 2,6-di-tert-butyl-4-methylphenol and 2,6-di-tert-butylphenol, Can. J. Chem. 41 (1963) 2807.
[47] P.V. Krasovskii, O.S. Malinovskaya, A.V. Samokhin, Y.V. Blagoveshchenskiy, V.A. Kazakov, A.A. Ashmarin, XPS study of surface chemistry of tungsten carbides nanopowders produced through DC thermal plasma/hydrogen annealing process, Appl. Surf. Sci. 339 (2015) 46.
[48] F.Y. Xie, L. Gong, X. Liu, Y.T. Tao, W.H. Zhang, S.H. Chen, H. Meng, J. Chen, XPS studies on surface reduction of tungsten oxide nanowire film by Ar+ bombardment, J. Electron Spectrosc. Relat. Phenom. 185 (2012) 112.
[49] R. Azimirad, P. Khosravi, A.Z. Moshfegh, Influence of hydrogen reduction on growth of tungsten oxide nanowires, J. Exp. Nanosci. 7 (2012) 597.
[50] X.Z. Zeng, Y.J. Zhou, S.D. Ji, H.J. Luo, H.L. Yao, X. Huang, P. Jin, The preparation of a high performance near-infrared shielding Cs_xWO_3/SiO_2 composite resin coating and research on its optical stability under ultraviolet illumination, J. Mater. Chem. C 3 (2015) 8050.